

# Principles of Magnetic Levitation Force and Motor Torque Generation by Superposition of Harmonics in Bearingless Brushless Motors

Franz Zürcher<sup>1</sup>, Thomas Nussbaumer<sup>2</sup>, Johann W. Kolar<sup>1</sup>

<sup>1</sup>Power Electronic Systems Laboratory, ETH Zürich,

<sup>2</sup>Levitronix GmbH  
zurcher@ieee.org

**Abstract**—In this paper the principles of motor torque and suspension force generation in bearingless brushless motors with high pole numbers are explained, graphically illustrated and analyzed in detail. The necessary harmonic components of the flux density in the air-gap are calculated and it is visualized how these can be generated by superposition of harmonics depending on a specific rotor pole / stator slot ratio. Especially, for bearingless motors with a fractional pole / slot ratio, it is shown how superior suspension performance and high rotational speeds can be achieved. The considerations are exemplified for a 26-pole / 24-slots bearingless brushless motor.

## I. INTRODUCTION

The popularity of permanent magnet bearingless brushless motors is constantly increasing in a broad band of applications [1]. Since no lubricants are needed and no wear of friction is occurring, they need only very little maintenance, which makes them suitable for applications like vacuum and fluid pumps in chemical, pharmaceutical and semiconductor industries. Additionally, bearingless motors are dedicated in applications under extreme conditions like space technology, where any lubricants would evaporate due to the vacuum [2], biochemical industry where an ultra high cleanliness has to be guaranteed [3] or energy storage by flywheels where friction losses have to be avoided [4]. In all these mentioned applications bearingless motors are profitable despite of their higher costs and system complexity compared to classical mechanical bearings.

Different bearingless motor concepts have been proposed so far [5]-[8], whereby for most of the aforementioned applications a very promising concept is the bearingless brushless slice motor as proposed in [9] due to its superior performance results. Thanks to its passive stabilization of the axial displacement and tilting, a highly compact setup can be achieved. For large rotor dimensions this concept can be realized by a high number of rotor poles  $2 \cdot p$  combined with a fractional ratio of the number of stator slots  $q$  and rotor poles [10]. While the motor torque is generated by a sinusoidal air-gap flux distribution with a frequency component at

$$f_{drv} = f_{mech} \cdot p, \quad (1)$$

a resulting suspension force can be generated by an air-gap

flux-density distribution, which exhibits a frequency component at

$$f_{bng} = f_{mech} \cdot (p \pm 1), \quad (2)$$

as described in [11]. These flux-density components can be generated by a suitable harmonic wave originating from the winding scheme in combination with the harmonics generated by the  $q$ -slotted stator teeth, as will be shown in this paper.

The physical and mathematical principles of force and torque generation in this motor type are basically known and described in literature. Different methods and models have been introduced to help to design and understand bearingless motors. However, a successful practical motor design is very hard to achieve based on the existing literature due to the high level of complexity associated with the bearingless motor concept. Especially, no illustrative explanation is given on how the different harmonics of the stator field and the rotor field may generate resulting radial suspension and tangential motor forces. In particular, no mathematical explanation for polyphase bearingless motors with a high number of rotor pole-pairs and stator slots has been presented so far.

In this paper an exemplary configuration with  $2 \cdot p = 26$  rotor poles,  $q = 24$  stator slots,  $m_{drv} = 3$  motor drive phases as well as  $m_{bng} = 3$  bearing phases has been chosen, which is used to explain and visualize the principles. It is shown in a comprehensible manner, how the magnetic field density distribution originating from a stator winding configuration placed in a certain number of stator slots may lead to a simultaneous suspension force and motor torque due to its interaction with the permanent magnet rotor field. In particular, it will be shown analytically and graphically how the harmonics of the required fields are generated and how the radial suspension force and the motor torque can be controlled in an independent and decoupled manner by appropriate winding schemes.

Although all the explanations in this paper are based on mathematical and physical principles, for sake of simplicity, some assumptions are made, namely:

- 1) Only forces acting in the  $xy$ -plane of a cross-section through the rotor and stator are considered, while axial and tilting degrees of freedom are assumed to be stabilized. This can be achieved by combining two bearingless motor units and an additional thrust bearing as proposed in [12] and illustrated in Fig. 1(a) or

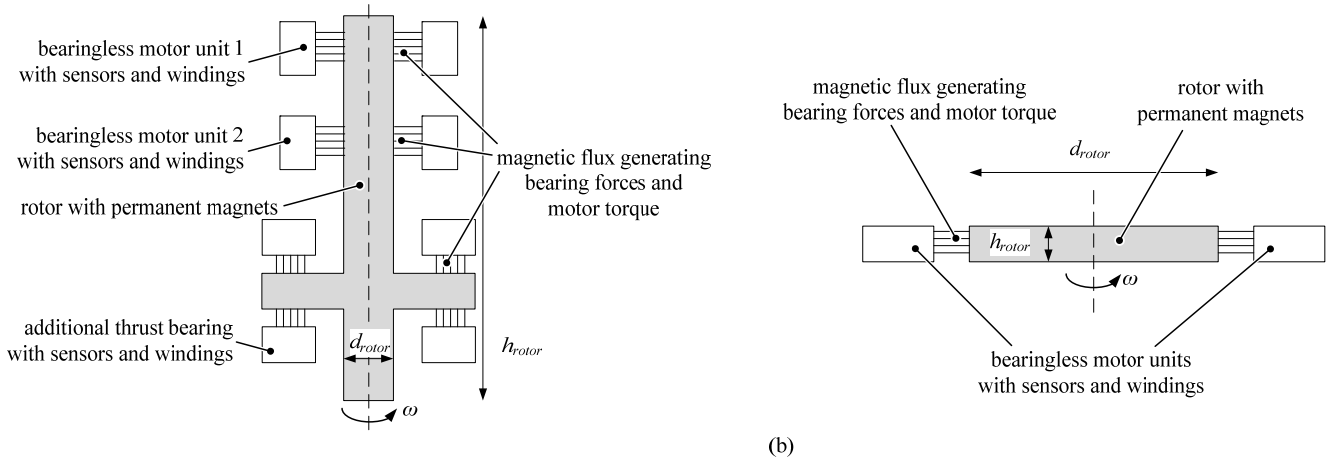


Fig. 1. Different bearingless motor concepts: the bearingless motor concept with two radial motor bearing units and an additional thrust bearing (a); and the bearingless slice motor concept with  $d_{rotor} \gg h_{rotor}$  and passive tilting and axial stabilization by reluctance forces (b) according to [9].

alternatively by using an auxiliary passive bearing such as introduced in [9] and depicted in Fig. 1(b). The latter concept is called bearingless slice motor and is used for the prototype to verify the calculations in this paper.

- 2) Only forces acting perpendicularly to the rotor or stator-teeth surfaces, respectively, are considered. This simplification can be made due to the high relative permeability  $\mu_{Fe}$  of the stator iron compared to the relative permeability  $\mu_0$  in the air-gap.
- 3) A very simple model of the resulting air-gap flux density distribution caused by the motor drive and bearing windings, respectively, will be introduced (cf. (7) and Fig. 5). This model has been verified by 3D FEM simulations. According to the results it can be used without loss of generality for the considered types of motors.
- 4) Only one winding type (bearing or drive) per tooth is considered, i.e. the bearing and motor windings are located on different teeth.
- 5) The flux density caused by the radial magnetized rotor permanent magnets is supposed to be perfectly sinusoidal. Due to measurements, which have been made, this can be assumed without loss of precision.

Although these assumptions and simplifications have been made, the proposed model and illustrations can be generalized and adapted for future concepts with a different number of rotor poles and a different stator topology.

## II. FORCE COMPONENTS IN BEARINGLESS BRUSHLESS MOTORS

In order to understand and visualize the appearing forces in the  $xy$ -plane of a bearingless motor, the forces, which are acting on the rotor, can be divided into two components, namely a radial and a tangential part  $F_{rad}$  and  $F_{tan}$ , respectively, with respect to the outer rotor surface. Since the relative permeability of the stator iron teeth  $\mu_{Fe}$  is very high compared to the relative permeability  $\mu_0$  in the air-gap, only forces acting perpendicularly to the rotor and stator-teeth surface are considered.

### A. Radial force components

The radial force components  $dF_{rad}$ , which are commonly denominated as Maxwell force components, are caused by the different relative permeabilities  $\mu_0$  of the air-gap and  $\mu_{Fe}$  of the stator iron. The magnitude of the components  $dF_{rad}$  is

proportional to the square of the total magnetic flux density in the air-gap, which is caused by the rotor permanent magnets and the additional flux density produced by the current flowing in the stator windings. Therefore, the radial force components  $dF_{rad}$  are always attracting the rotor to the stator teeth and only the magnitude can be influenced by an appropriate winding current. Simplified, the components  $dF_{rad}$  can be calculated in dependency on the rotor angle  $\varphi$  according to

$$dF_{rad} = \frac{B_{tot}(\varphi)^2 \cdot h \cdot r \cdot d\varphi}{2 \cdot \mu_0} = \frac{(B_{pm}(\varphi) + B_{wdg}(\varphi))^2 \cdot h \cdot r \cdot d\varphi}{2 \cdot \mu_0}, \quad (3)$$

where  $B_{tot}$  is the total magnetic flux density in the air-gap, consisting of the flux density  $B_{pm}$  caused by the rotor permanent magnets and the flux density  $B_{wdg}$ , caused by the currents in the stator windings,  $h$  is the rotor and stator height and  $r$  is the inner radius of the stator teeth.

As the radial Maxwell force components  $dF_{rad}$  always act perpendicularly to the rotor surface, they can never generate a torque on the rotor as can be seen in Fig. 2(a) and 3(a). But as will be seen later, they can be used to generate a resulting radial force, which is used for the bearingless levitation of the rotor as shown in Fig. 3(a).

### B. Tangential force components

The tangential force components can be calculated by the formula known as the Lorentz-force. According to [13] this formula can be applied despite the fact that the concentrated windings are placed in the stator slots, where virtually no permanent magnet field occurs. Instead, there are Maxwell force components, which act perpendicularly to the inner side of the stator teeth, and therefore generate a resulting lateral force on the rotor. In [13] it is shown that the following equation (4) can be used nevertheless and the virtual Lorentz force calculated in this manner is exactly equal to the sum of the real but small Lorentz force plus the lateral Maxwell force. Thus, the tangential force components  $dF_{tan}$  can simply be calculated according to

$$dF_{tan} = (B_{pm} \cdot dl_{wdg}) \cdot I_{wdg}, \quad (4)$$

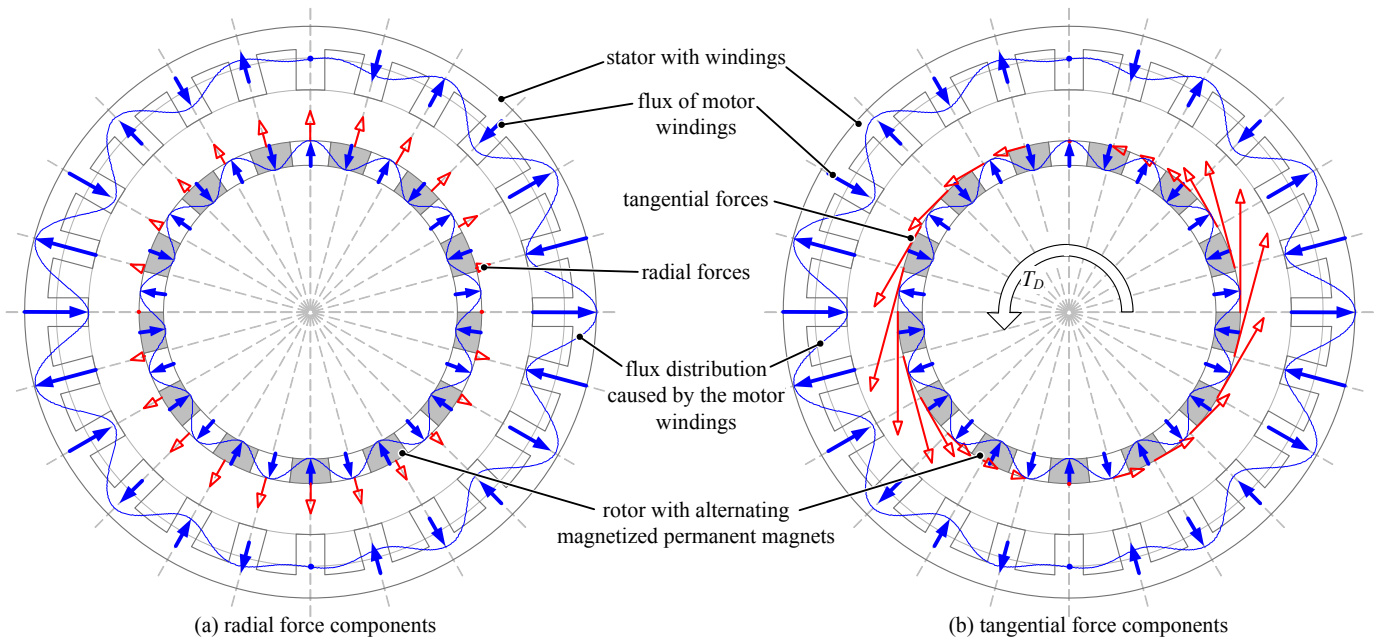


Fig. 2. Motor winding: A torque is generated by tangential forces (b) while the radial forces (a) cancel each other, thus no radial force is resulting.

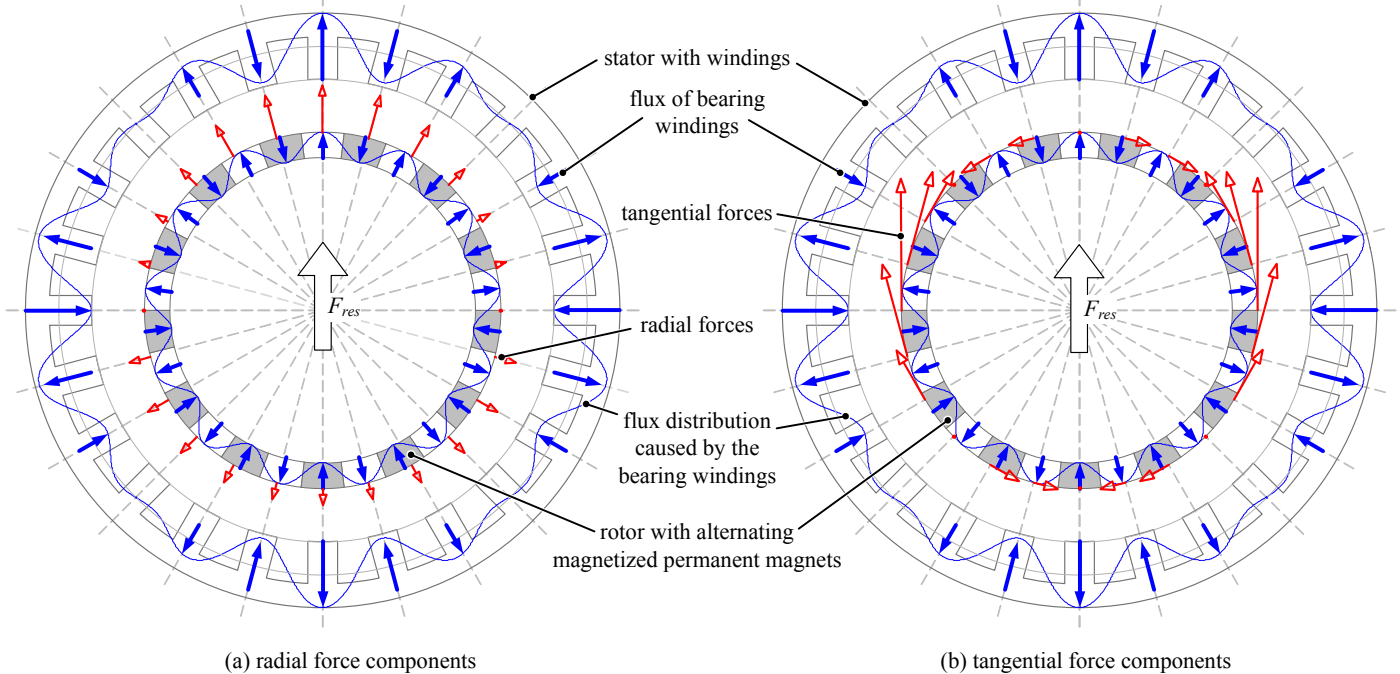


Fig. 3. Bearing winding: A resulting suspension force is generated by radial forces (a) as well as by tangential forces (b), both pointing in the same direction.

where  $B_{pm}$  is the radial flux caused by the rotor permanent magnets,  $dl_{wdg}$  is a length element of the windings in the magnetic field region and  $I_{wdg}$  is the current flowing in the corresponding windings. As the magnitude of  $dF_{tan}$  is proportional to the winding current, tangential force components pointing in either clockwise or counterclockwise directions can easily be generated and controlled by applying a corresponding current in the windings.

The tangential force components can sum up to a resulting torque, as shown in Fig. 2(b), but they can also be used to generate a resulting suspension force if always the two opposite force components point in the opposite lateral direction as shown in Fig. 3(b).

### III. TORQUE AND SUSPENSION FORCE GENERATION BY INTERACTION OF HARMONIC FIELDS

#### A. Torque generation by tangential force components

The motor winding scheme of the exemplary configuration is depicted in Fig. 4(a). As will be shown in section IV, by this scheme an air-gap flux density distribution with a strong frequency component at the desired frequency  $f_{drv}$  can be generated, resulting in a torque on the rotor but no resulting radial force, which could deflect the rotor.

In Fig. 2(b) it can be seen that the tangential force components according to (4) sum up to a resulting motor torque if the order of the frequency component  $f_{drv} / f_{mech}$  of

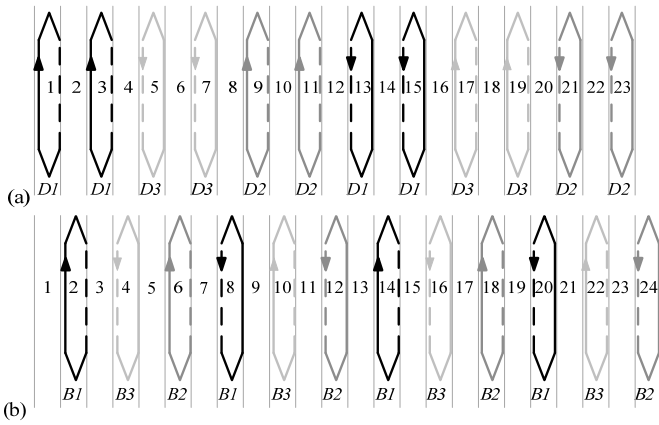


Fig. 4. Winding scheme of the motor drive (a) and bearing (b) windings.

the air-gap flux density distribution is equal to the number the rotor pole-pairs  $p$ , which in the illustrated exemplary configuration is:

$$\frac{f_{drv}}{f_{mech}} = p = 13. \quad (5)$$

Thus, a resulting torque is generated by the interaction of the two flux densities  $B_{pm}$  caused by the rotor permanent magnets and  $B_{drv}$  caused by the motor drive windings, both containing a frequency component with a significant magnitude at  $f_{drv} = f_{mech} \cdot p$ .

The radial force components calculated according to (3) can obviously never contribute to the motor torque, as they have no tangential part by definition. Also the radial force components generated by the motor drive windings do not generate a resulting radial force on the rotor, as always the two opposite force components cancel each other out as can be seen in Fig. 2(a).

#### B. Suspension force generation by tangential and radial force components

The bearing winding scheme, which is used to generate the levitation force, is depicted in Fig. 4(b) for the exemplary configuration. By this winding scheme, which is different from the motor drive winding scheme, an air-gap flux distribution with other frequency components is generated. In section IV it will be shown that a strong frequency component in this exemplary case occurs at:

$$\frac{f_{bng}}{f_{mech}} = p + 1 = 14. \quad (6)$$

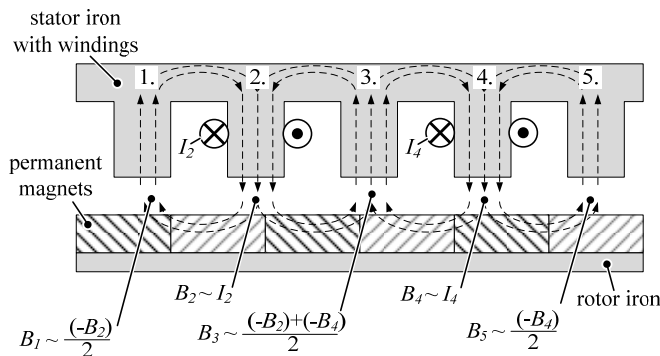


Fig. 5. Simplified model of the magnetic flux density distribution caused by the winding currents  $I_2$  and  $I_4$ .

Since this fulfils (2), a resulting radial force is generated. In Fig. 3(a) and 3(b) it is visualized that both the radial Maxwell force components according to (3) as well as the tangential Lorentz force components according to (4) sum up to a resulting force, both pointing to the same direction. On the other hand, no torque is generated, as always two force components contribute with the same magnitude but different signs to the total torque, thus cancel each other out.

If  $p+1$  in (6) would be replaced by  $p-1$ , the two resulting forces in Fig. 3(a) and Fig. 3(b) would point to opposing directions and would partially cancel each other for inner rotor constructions.

#### IV. GENERATION OF HARMONIC FIELDS BY WINDING CURRENTS

As shown before, a motor torque can be generated by a sinusoidal flux-density with  $f_{drv} = f_{mech} \cdot p$ , while a resulting suspension force can be generated by a flux-density with frequency a component at  $f_{bng} = f_{mech} \cdot (p \pm 1)$ . These flux-densities are generated by a suitable harmonic wave generated by an appropriate winding scheme and the harmonics generated by the  $q$ -slotted stator teeth.

For the calculation of the resulting air-gap flux density distribution in bearingless motors with large air-gap and large radial permanent magnets length with respect to the rotor back iron thickness, a simple model can be used, which is illustrated in Fig. 5:

- 1) The flux density  $B_n$  in front of each stator tooth is assumed to be proportional to the current  $I_n$  flowing in the corresponding windings wound around this tooth.
- 2) The flux density in front of a tooth with no correspondent winding current is composed of half the negative sum of the flux densities of both of its direct neighbors, e.g. the flux density  $B_n$  in front of the tooth  $i$  is equal to:

$$B_n = \frac{(-B_{n-1}) + (-B_{n+1})}{2}. \quad (7)$$

This assumption can be made because only a small amount of the flux generated by the windings enters the rotor iron due to the large air-gap plus the surface-mounted permanent magnet length (with air-like permeability) compared to the rotor iron thickness. Additionally, the rotor iron is mostly saturated by the permanent magnet flux.

Thus, the flux of a single winding returns via the two direct neighbor-teeth of the originating tooth. This fact has been verified by 3D FEM simulations for the exemplary configuration. Fig. 6 shows the flux distribution of a current

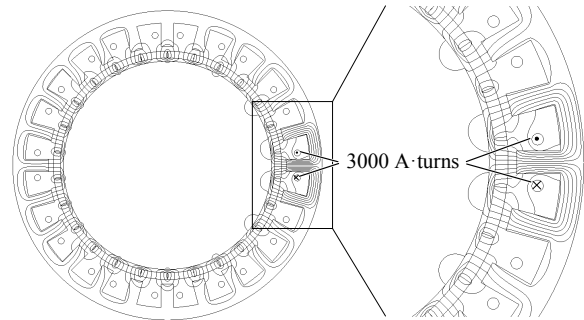


Fig. 6. 3D FEM simulation results of the flux distribution of one single winding with  $I_{wdg} = 3000 \text{ A} \cdot \text{turns}$ .

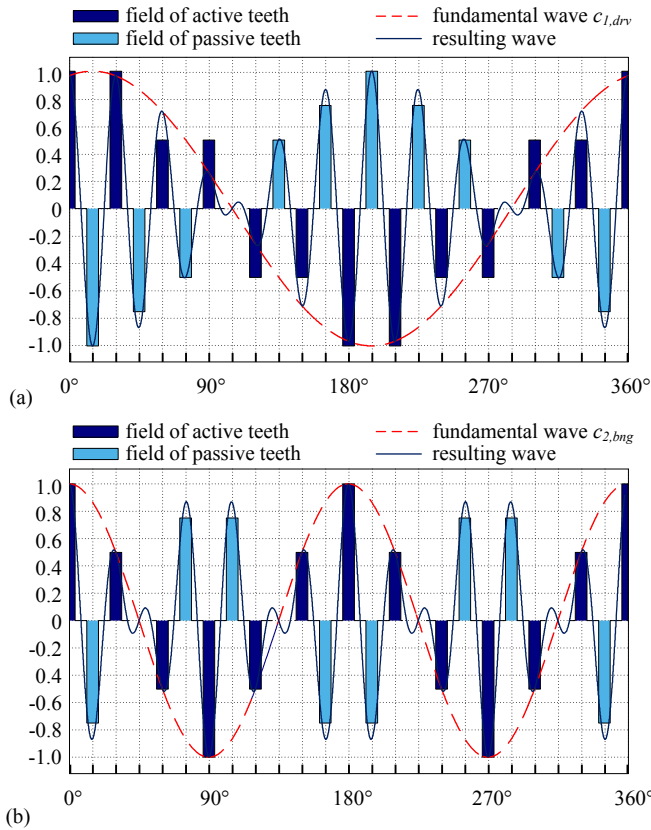


Fig. 7. Current distribution of active and passive stator teeth and fundamental harmonic of the motor drive (a) and bearing (b) windings.

$I = 3000$  A·turns flowing in a single winding wound around one of the stator teeth. It can be seen that the winding current does not influence the air gap flux but in front of the specific tooth and its direct neighbors. The flux in front of the other stator teeth is influenced only by the permanent magnets of the rotor. This allows a very easy way to calculate the air-gap flux.

The total resulting flux density is calculated as a composition of two sine-waves, a harmonic wave with order  $c_1$  caused by the  $q$ -slotted stator teeth and a wave  $c_2$  generated by an appropriate winding scheme, which is different for the motor drive and bearing windings. As the motor drive and bearing teeth are splitted alternately, and thus only every second tooth is used for the motor drive or bearing windings, respectively, the order of  $c_1$  is equal to  $q/2$ .

According to the well-known equation

$$\sin(\alpha) \cdot \sin(\beta) = \frac{\cos(\alpha - \beta) - \cos(\alpha + \beta)}{2}, \quad (8)$$

the resulting flux density in dependency on the angle  $\varphi$  is proportional to

$$B(\varphi) \sim \sin(c_1 \cdot \varphi) \cdot \sin(c_2 \cdot \varphi) = \frac{\cos((c_1 - c_2) \cdot \varphi) - \cos((c_1 + c_2) \cdot \varphi)}{2}. \quad (9)$$

Therefore, the resulting flux density exhibits harmonic components with the order  $(c_1 - c_2)$  and  $(c_1 + c_2)$ . In the following, the harmonic flux density components will be calculated for the drive and the bearing system.

#### A. Motor windings of the exemplary configuration

As explained in section III.A, the required stator field for the generation of a motor torque must have the same number

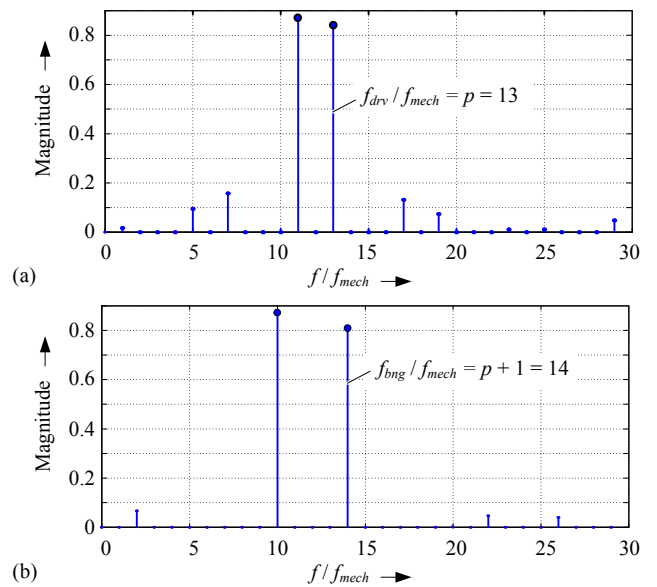


Fig. 8. Harmonic components of the field generated by the motor (a) and bearing (b) windings.

of poles  $2 \cdot p = 26$  as the rotor with its 26 permanent magnets. As before mentioned, this is achieved by the modulation of the harmonic wave with order  $c_1 = q/2 = 12$  generated by the  $q$  stator slots and a sine-wave with the order  $c_2,drv = 1$  generated by the appropriate drive winding scheme depicted in Fig. 4(a).

According to (7) and (9) the resulting flux density distribution  $B(\varphi)$  of the motor drive windings along the circumferential angle  $\varphi$  is proportional to:

$$B_{drv}(\varphi) \sim \sin(12 \cdot \varphi) \cdot \sin(\varphi) = \frac{\cos(11 \cdot \varphi) - \cos(13 \cdot \varphi)}{2}. \quad (10)$$

Thus, the  $p^{th}$  harmonic with  $f_{drv} / f_{mech} = p = 13$  is generated. The flux in front of the active and passive stator teeth, generated by the drive windings (cf. Fig. 4(a)) is depicted in Fig. 7(a). Interestingly, the 13<sup>th</sup> harmonic component of the resulting flux density is not directly visible. But a frequency analysis of the air-gap flux distribution (cf. Fig. 8(a)) shows that a frequency component with order  $p = 13$  occurs as calculated before, which leads, by interaction with the rotor permanent magnets, to a resulting torque as shown in Fig. 2(b).

#### B. Bearing windings of the exemplary configuration

To create a resulting radial force, a stator field with the number of poles equal to the number of rotor pole pairs  $p \pm 1$  has to be generated, as explained in section III.B. Therefore, for the exemplary configuration with an inner rotor there have to be  $p + 1 = 14$  pole pairs to have both, the tangential and radial force components, summing up in a resulting force pointing in the same desired direction.

The flux density distribution of the bearing system can be calculated analog to the calculations for the drive system in section IV.A. The order of the harmonic wave, which is generated by the bearing windings depicted in Fig. 4(b), is  $c_2,bng = 2$ . Using (7) and (9) the resulting flux density  $B_{bng}(\varphi)$  of the bearing system along the circumferential angle

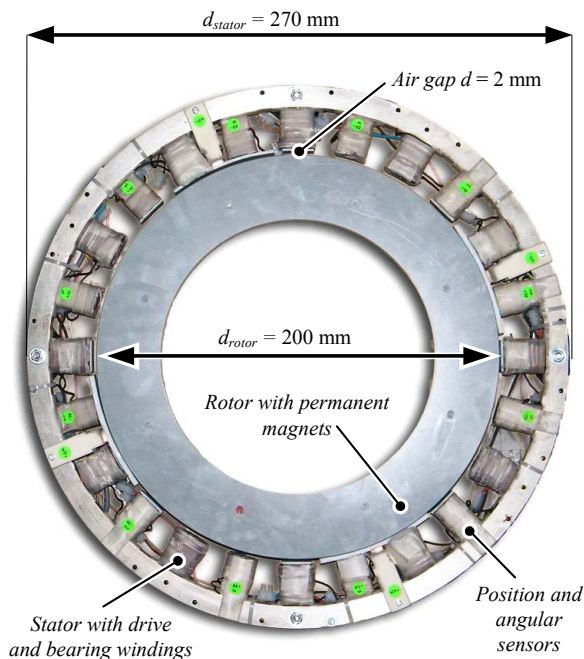


Fig. 9. Photo of the experimental prototype.

$\varphi$  can be calculated proportional to

$$B_{bng}(\varphi) \sim \sin(12 \cdot \varphi) \cdot \sin(2 \cdot \varphi) = \frac{\cos(10 \cdot \varphi) - \cos(14 \cdot \varphi)}{2} \quad (11)$$

Therefore, the bearing windings shown in Fig. 4(b) generate the  $(p+1)^{\text{th}}$  harmonic with  $f_{bng}/f_{mech} = (p+1) = 14$ , which produces, in interaction with the rotor permanent magnet flux, a resulting radial force acting on the rotor. Fig. 7(b) shows the resulting flux density distribution. Again the relevant harmonic wave with order  $(p+1)$  is not directly visible, but can be seen in the analytical frequency analysis shown in Fig. 8(b).

## V. EXPERIMENTAL VERIFICATION

A laboratory prototype has been built to verify the assumptions and the simplified model. As proposed the number of rotor poles has been chosen as  $2 \cdot p = 26$ , the number of stator slots / teeth as  $q = 24$  and the number of bearing as well as motor drive phases as  $m_{bng} = m_{drv} = 3$ . A photo of the prototype is depicted in Fig. 9, where also the main parts are labeled. With an appropriate control algorithm and a power electronics inverter the rotor can be levitated contactlessly.

The prototype system has been designed for a target maximal rotational speed of 15000 r/min, which is challenging in terms of the bearing control algorithm and signal path requirements due to the high electrical frequencies caused by the high number of rotor pole pairs  $p = 13$ . In addition, a stable bearing at such high speeds demands very precise position and angular sensors.

With the laboratory prototype radial suspension forces up to  $F_{max} = 350$  N in every desired direction can be generated.

The most important parameters and experimental measured properties of the prototype are listed in Table I.

TABLE I  
PROPERTIES AND EXPERIMENTAL RESULTS OF THE PROTOTYPE

| Parameter                       | Symbol       | Value | Unit  |
|---------------------------------|--------------|-------|-------|
| Number of stator teeth / slots  | $q$          | 24    |       |
| Number of drive teeth           | $q_{drv}$    | 12    |       |
| Number of bearing teeth         | $q_{bng}$    | 12    |       |
| Number of rotor poles           | $2 \cdot p$  | 26    |       |
| Number of bearing phases        | $m_{bng}$    | 3     |       |
| Number drive phases             | $m_{drv}$    | 3     |       |
| Target maximum rotational speed | $n_{r,max}$  | 15000 | r/min |
| Permanent magnet length         | $l_{magnet}$ | 10    | mm    |
| Stator iron height              | $h_{stator}$ | 40    | mm    |
| Stator outer diameter           | $d_{stator}$ | 270   | mm    |
| Rotor outer diameter            | $d_{rotor}$  | 200   | mm    |
| Mechanical air-gap              | $\delta$     | 2     | mm    |
| Maximum bearing force           | $F_{max}$    | 350   | N     |

## VI. CONCLUSION

In this paper the principles of motor torque and suspension force generation in bearingless brushless motors are explained and analyzed. Although the illustrations and analytically calculated examples are given for an exemplary configuration, the explanations can easily be generalized and be used for future developments of bearingless brushless motors with different stator slot / pole-pair combinations. Even an adaption for motors with outer rotors can simply be derived from the presented equations. The results have been verified with a laboratory prototype using the presented exemplary configuration.

## REFERENCES

- [1] A. Salazar, A. Chiba, T. Fukao, "A review of development in bearingless motors," *7th Int. Symp. on Magn. Bearings, Zurich, Switzerland*, Aug. 23-25, 2000, p. 335-340.
- [2] Y. Chisti and M. Moo-Young, "Clean-in-place systems for industrial bioreactors: Design, validation and operation," *Journal of Industrial Microbiology and Biotechnology*, vol. 13, p. 201-207, July 1994.
- [3] J. Zhou and K. Tseng, "A disk-type bearingless motor for use as satellite momentum-reaction wheel," *33rd Annual IEEE Power Electronics Specialists Conference*, 2002. PESC02, p. 1971-1975.
- [4] K. Asami, A. Chiba, M. Rahman, T. Hoshino, and A. Nakajima, "Stiffness analysis of a magnetically suspended bearingless motor with permanent magnet passive positioning," *IEEE Transactions on Magnetics*, vol. 41, 2005, p. 3820-3822.
- [5] G. Yang, Z. Deng, X. Cao, and X. Wang, "Optimal winding arrangements of a bearingless switched reluctance motor," *IEEE Trans. Power Electron.*, vol. 23, no. 6, pp. 3056-3066, Nov. 2008.
- [6] P. Karutz, T. Nussbaumer, W. Gruber, and J. W. Kolar, "Novel magnetically levitated two-level motor," *IEEE/ASME Trans. Mechatron.*, vol. 13, no. 6, pp. 658-668, Nov. 2008.
- [7] N. Watanabe, H. Sugimoto, A. Chiba, T. Fukao, and M. Takemoto, "Basic characteristic of the multi-consequent-pole bearingless motor," in *Proceedings PCC, Nagura*, 2007, pp. 1565-1570.
- [8] A. Chiba, D. Power, and M. Rahman, "Characteristics of a bearingless induction motor," *IEEE Trans. Magn.*, vol. 27, pt. 6, pp. 5199-5201, Nov. 1991.
- [9] R. Schoeb and N. Barletta, "Principle and application of a bearingless slice motor," *JSME Int. J. Series C*, vol. 40, pp. 593-598, 1997.
- [10] F. Zürcher, T. Nussbaumer, W. Gruber and J. W. Kolar, "Novel bearingless fractional slot motor," *IEEE International Magnetics Conference 2009*, Sacramento CA, USA, May 4-9, 2009.
- [11] S. Silber, W. Amrhein, P. Bosch, R. Schob, and N. Barletta, "Design aspects of bearingless slice motors," *IEEE/ASME Transactions on Mechatronics*, vol. 10, 2005, p. 611-617.
- [12] Q. Hijikata, S. Kobayashi, M. Takemoto, Y. Tanaka, A. Chiba, and T. Fukao, "Basic characteristics of an active thrust magnetic bearing with a cylindrical rotor core," *IEEE Trans. Magn.*, vol. 44, no. 12, pp. 4167-4170, Dec. 2008.
- [13] K. Küpfmüller, "Einführung in die theoretische Elektrotechnik," 14. Auflage, Springer Verlag Berlin, 1993, p. 332